SCIEPublish

Article

Investigation of Structure of the High-Entropy Alloy $Al_{0.5}CoCrCuFeNi$

Yuri Semerenko [1,*], Vasilij Natsik [1], Nikolai Galtsov [1], Diana Hurova [1], Victor Zoryansky [1], Elena Tabachnikova [1], Tamara Bednarchuk [2], Igor Kolodiy [3] and Peter Zinoviev [1]

[1] B.Verkin Institute for Low Temperature Physics and Engineering of the National Academy of Sciences of Ukraine, 47 Nauky Ave., 61103 Kharkiv, Ukraine; natsik@ilt.kharkov.ua (V.N.); galtsov@ilt.kharkov.ua (N.G.); hurova@ilt.kharkov.ua (D.H.); zoryansky@ilt.kharkov.ua (V.Z.); tabachnikova@ilt.kharkov.ua (E.T.); zinoviev@ilt.kharkov.ua (P.Z.)

[2] Institute of Low Temperature and Structure Research, Polish Academy of Sciences, P.O. Box 1410, 50-950 Wroclaw, Poland; t.bednarchuk@intibs.pl (T.B.)

[3] National Science Center Kharkiv Institute of Physics and Technology, 1 Akademicheskaya St., 61108 Kharkiv, Ukraine; kolodiy@kipt.kharkov.ua (I.K.)

* Corresponding author. E-mail: semerenko@ilt.kharkov.ua (Y.S.)

Received: 15 May 2025; Accepted: 2 September 2025; Available online: 11 September 2025

ABSTRACT: A detailed examination of the structure of the high-entropy alloy $Al_{0.5}CoCrCuFeNi$ at room temperature was carried out using different methods of optical microscopy, electron microscopy and X-ray structural analysis techniques. Numerical estimates of the dislocation density $\sim 5 \cdot 10^{15}$ m^{-2}, the mean size of the ordered (crystalline) domains ~ 18 nm and lattice micro strain $\sim 3 \cdot 10^{-3}$ were obtained through Williamson-Hall analysis of XRD patterns. The estimates of the dislocation density were found to correlate with the estimates of the total length of dislocation segments per unit volume, which effectively interact with elastic vibrations of the sample $\sim 4 \cdot 10^{13}$ m^{-2}, as previously determined from acoustic relaxation measurements. This is consistent with the idea that a significant portion of dislocations are concentrated in grain boundaries, and only dislocation segments located inside grains and having a favourable orientation with respect to the direction of sound wave propagation can effectively interact with cyclic deformation of the sample.

Keywords: High entropy alloy $Al_{0.5}CoCrCuFeNi$; Electron microscopy and X-ray structural analysis; Dislocation structure

1. Introduction

High-Entropy Alloys (HEAs) are complex metallic systems composed of five or more elements with nearly equiatomic concentrations. In most cases, HEAs form single-phase solid solutions with face-centered cubic (FCC) or body-centered cubic (BCC) crystal structures [1–4]. Due to the incorporation of chemically and structurally diverse elements, these lattices undergo significant distortion [5–8], which in turn influences their mechanical properties, phase stability, and potential functional applications.

These alloys exhibit significantly higher mixing entropy ΔS_{mix} than conventional multi-component alloys, which is the basis for their name [1].

According to Boltzmann's hypothesis, the mixing entropy of an n element regular solution alloy is determined by the Gibbs entropy formula:

$$\Delta S_{mix} = -R\sum_{i=1}^{n} C_i \ln C_i \,, \tag{1}$$

where C_i is the mole percent of the component and $\sum_{i=1}^{n} C_i = 1$.

https://doi.org/10.70322/amsm.2025.10012

The explanation for the increased value of entropy in HEA is based on the concept of thermodynamics, which states that the entropy of mixing between soluble components is maximum when these components are in equiatomic concentration [9]. In this case:

$$\Delta S_{mix} = R \ln n, \tag{2}$$

where R is the gas constant, and n is the number of components. Thus mixing entropy ΔS_{mix} increases with the increasing number of components.

By various authors, HEAs are usually called multi-component alloys in which $\Delta S_{mix} \geq 1.5 \div 1.61$ [10].

The change in Gibbs free energy ΔG_{mix} when mixing HEA components is determined by the relation:

$$\Delta G_{mix} = \Delta H_{mix} - T\Delta S_{mix}, \tag{3}$$

where ΔH_{mix} is the change in enthalpy of mixing, T is the temperature.

The calculation of ΔH_{mix} is described by the following equation [10–12]:

$$\Delta H_{mix} = \sum_{i,j=1;\ i \neq j}^{n} 4 \cdot \Delta H_{mix}^{ij} C_i C_j, \tag{4}$$

where ΔH_{mix}^{ij} is defined as the mixing enthalpy of binary $i-j$ alloys in the liquid state.

Hence, the contribution of the entropy of mixing ΔS_{mix} during the formation of HEAs reduces the free energy ΔG_{mix}. As a result, the likelihood of forming substitutional solid solutions with simple crystal lattices (fcc and bcc) significantly increases. Such lattices are significantly distorted, because they are formed by atoms of different elements with varying electronic structures and atomic sizes.

Due to these features, the properties of HEAs compare favourably with the properties of traditional alloys obtained by alloying one base component: they have a favourable combination of strength and ductility, high resistance to thermal and mechanical influences and high corrosion resistance.

One of the most studied model systems of high-entropy alloys is $Al_xCoCrCuFeNi$; $x=0 \div 1$. It has been established that the phase composition of such alloys is determined by both the aluminum molar ratio x [12] and the solidification cooling rate [13].

In the case x = 0.5, HEA $Al_{0.5}CoCrCuFeNi$ tends to be predominantly single-phase with fcc lattice [13,14]. It has been established that for this alloy $\Delta H_{mix} = -1.52\ \frac{\text{kJ}}{\text{mol}}$, $\Delta S_{mix} = 14.7\ \frac{\text{J}}{\text{K·mol}}$ [13]; the ordering temperature is 968 K, the melting point of Cu-rich phase is 1426 K, the solidus temperature is 1552 K, and the liquidus temperature is 1635 K [12]. The melting points of the chemical components of the high-entropy alloy $Al_{0.5}CoCrCuFeNi$ are given in Table 1.

Table 1. Melting point of chemical components [13,15,16] and nominal compositions of high-entropy alloy $Al_{0.5}CoCrCuFeNi$.

Chemical Element	Al	Cr	Fe	Co	Ni	Cu
melting point, K	933	2180	1811	1768	1728	1358
nominal compositions of the HEA, at. %	9.091	18.1818	18.1818	18.1818	18.1818	18.1818

High-Entropy Alloys (HEAs), composed of multiple principal elements in near-equiatomic ratios, have garnered significant attention due to their exceptional mechanical strength, thermal stability, and corrosion resistance. These properties make HEAs highly attractive for the fabrication of complex metallic components via Additive Manufacturing (AM) technologies [17].

HEA $Al_{0.5}CoCrCuFeNi$, due to its outstanding mechanical performance and corrosion resistance, have emerged as promising candidates for manufacturing intricate metallic components via AM [18,19]. In particular, for Powder Bed Fusion (PBF) methods tailored for metal processing—such as Selective Laser Melting (SLM), Direct Metal Laser Sintering (DMLS), and Electron Beam Melting (EBM). These methods enable the fabrication of dense, high-strength structures with superior mechanical properties and complex geometries and high dimensional precision. Recent studies have shown that HEAs fabricated via SLM can achieve tensile strengths exceeding 1 GPa while maintaining ductility, thanks to refined grain structures and solid-solution strengthening [17,20].

Moreover, HEAs exhibit intrinsic biocompatibility and corrosion resistance, making them promising candidates for biomedical applications, including orthopedic implants and surgical tools. Their ability to maintain structural integrity in physiological environments positions them as viable alternatives to conventional titanium or cobalt-chromium alloys [17].

However, the phase composition and microstructure of HEAs are highly sensitive to processing parameters such as laser power, scan speed, and cooling rate. This sensitivity leads to significant variability in phase formation, grain morphology, and defect distribution. While several studies have explored these relationships [17–21], the current understanding remains incomplete, particularly regarding the interplay between AM-induced thermal gradients and phase stability.

Recent reviews have also highlighted the potential of Direct Energy Deposition (DED) techniques for producing large-scale HEA components with tailored compositions and gradient structures [20]. Additionally, binder jetting and material extrusion methods are being investigated for producing HEA green bodies that undergo sintering to achieve full density, expanding the design space for functional components [20].

Since the phase composition and microstructure of the $Al_{0.5}CoCrCuFeNi$ alloy highly depend on the conditions of obtaining the samples, cooling rate and post-processing treatments, grain morphology and defect structures) [13]. However, currently known studies [13,14,22] of its structure are still limited in scope and require further exploration to fully understand the structure—property relationships.

In this publication, we present a comprehensive analysis of HEA $Al_{0.5}CoCrCuFeNi$ samples produced under varying conditions, employing a combination of optical microscopy, scanning and transmission electron microscopy, and X-ray diffraction techniques. By correlating microstructural features with processing parameters, we aim to contribute to the growing body of knowledge on HEA behaviour in AM environments and support the development of optimized manufacturing strategies for next-generation metallic systems.

2. Material

The initial ingot of the multi-component alloy, composed of 4.46 wt.% aluminium, 19.48 wt.% cobalt, 21.02 wt.% copper, 17.18 wt.% chromium, 19.4 wt.% nickel, and 18.46 wt.% iron, was produced by remelting high-purity (≈99.9%) components on a copper water-cooled hearth in an arc furnace, utilizing a non-consumable tungsten electrode. The remelting process was conducted in the atmosphere of purified argon. To achieve a uniform distribution of elements, the alloy underwent five remelting cycles, with periodic turnover on the hearth.

It was decided to study the structural characteristics of not only the initial cast coarse-grained state (I), but also their characteristics after a series of long-term high-temperature annealings: (II)—after high-temperature annealing in vacuum at 1243 K for 6 h; (III)—high-temperature annealing at 1243 K for 6 h with subsequent annealing at 923 K for 6 h; (IV)—high-temperature annealing in vacuum at 1243 K for 6 h (the results were taken after 10 years of aging at room temperature after annealing). Annealing was performed in a vacuum. Following the annealing process, the samples were cooled along with the furnace at a rate of 4–5 degrees per minute until reaching 770 K. This choice of heat treatment modes is due to the fact that the mechanical and acoustic properties of the HEA $Al_{0.5}CoCrCuFeNi$ for structural states (I) and (IV) have been studied in detail in [23–28]. The scheme for obtaining the studied structural states (I)–(IV) is shown in Figure 1.

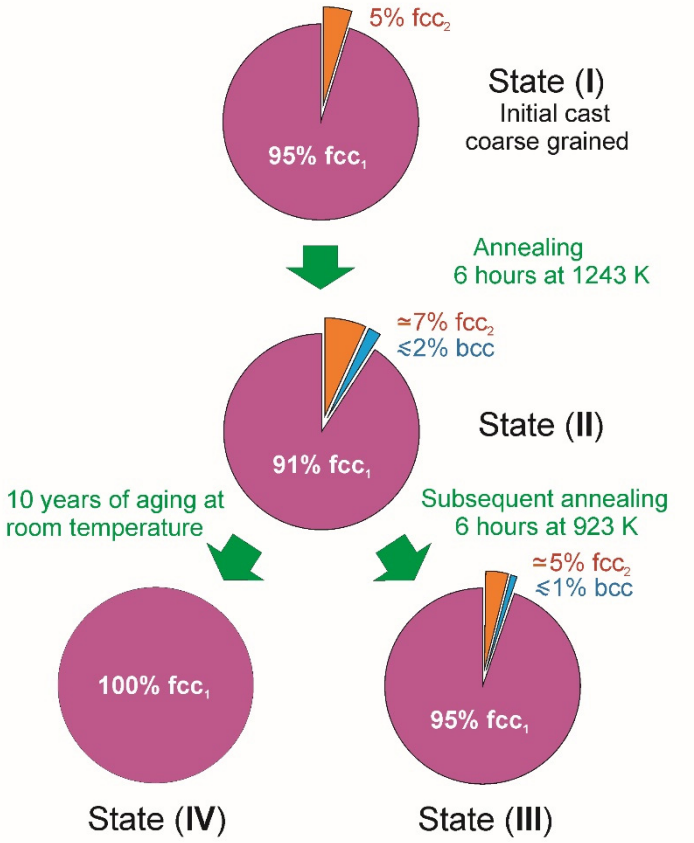

Figure 1. The scheme for obtaining the studied structural states (I)–(IV) of high-entropy alloy $Al_{0.5}CoCrCuFeNi$.

The metallographic analysis [24] presented in Figure 2 reveals that the microstructure of the alloy in the initial state (I) exhibits a characteristic dendritic pattern, consisting primarily of a dense body of dendrites as the main structural component, along with interdendritic spaces. Such a crystallographic texture inevitably forms when creating blanks from alloys using the argon-arc method with directed heat removal.

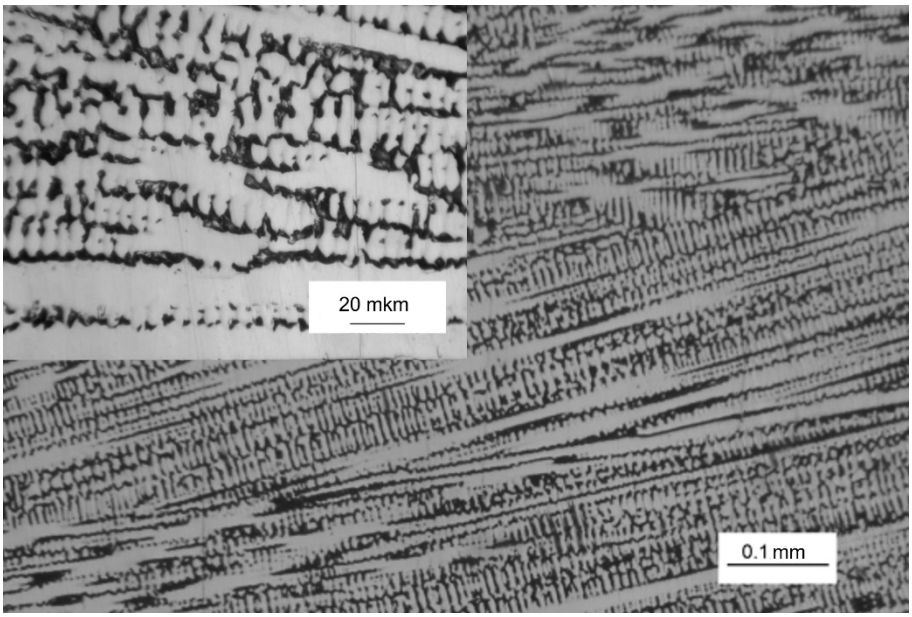

Figure 2. Microstructure of a sample of high-entropy alloy $Al_{0.5}CoCrCuFeNi$ in the initial cast state (I). The inset shows the structure on a larger scale.

The elemental composition of the obtained ingots was studied by energy dispersive X-ray spectroscopy (EDS). Two samples (**A** and **B**) cut from different neighbouring regions of the ingot of the high-entropy alloy $Al_{0.5}CoCrCuFeNi$ in structural state (II) were examined.

Figure 3 shows the results of determining the elemental composition of the alloy under study. The electron microscopy imaging of the sample and its elemental composition were studied using a Field Emission Scanning Electron Microscope (FE-SEM) FEI Nova Nano SEM 230 (Hillsboro, OR, USA) a Quanta 3D FEG (Quanta, Hillsboro, OR, USA) systems along with energy dispersive X-ray spectrometer EDAX Genesis XM4 (EDAX Inc., Mahwah, NJ, USA).

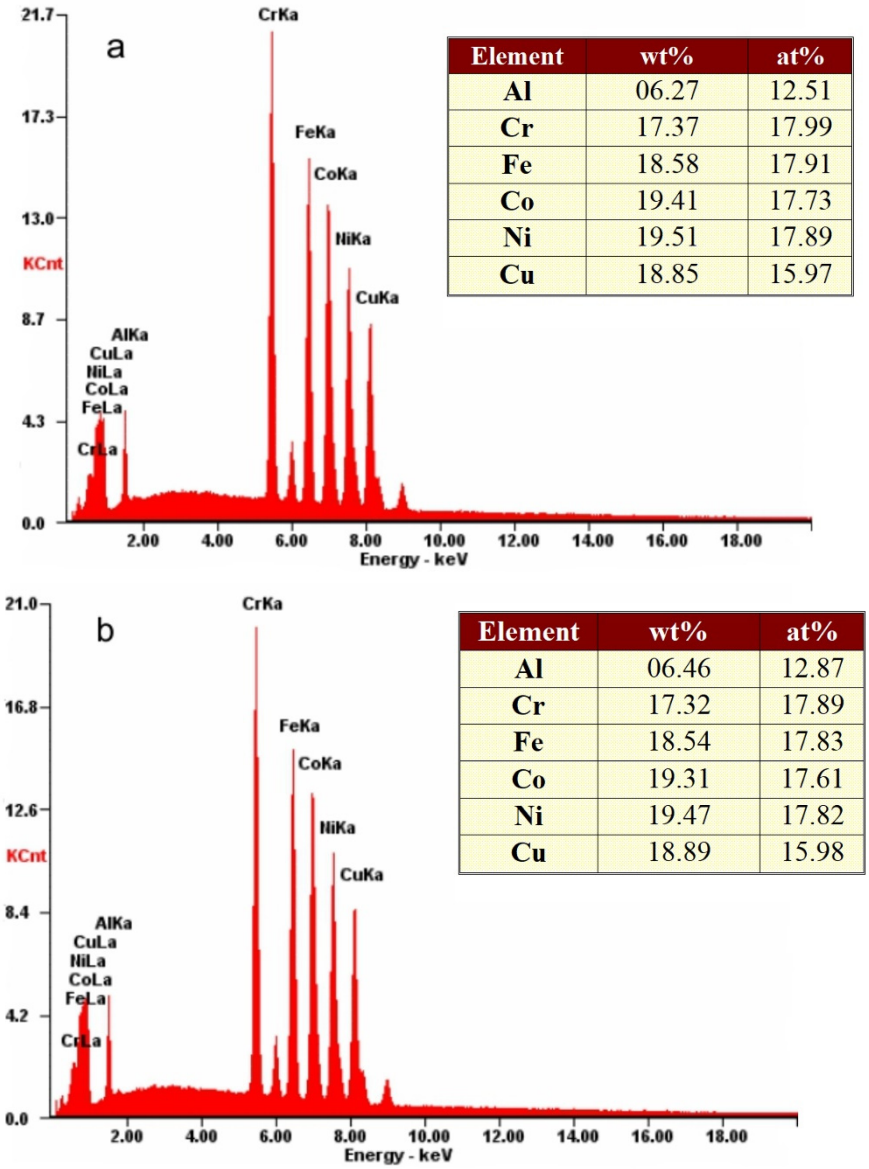

Element	wt%	at%
Al	06.27	12.51
Cr	17.37	17.99
Fe	18.58	17.91
Co	19.41	17.73
Ni	19.51	17.89
Cu	18.85	15.97

Element	wt%	at%
Al	06.46	12.87
Cr	17.32	17.89
Fe	18.54	17.83
Co	19.31	17.61
Ni	19.47	17.82
Cu	18.89	15.98

Figure 3. The EDS patterns for the high-entropy alloy $Al_{0.5}CoCrCuFeNi$ in structural state (II): (**a**,**b**)—pattern for two different regions of the ingot (**A** and **B**, respectively).

It was found that the composition of the two samples studied differs slightly. These data correlate with the presence of dendritic structure (see Figure 2) and may indicate the presence of noticeable differences in the elemental chemical composition of dendrites and interdendritic spaces.

3. Results and Discussion

3.1. Dendritic Structure of the High-Entropy Alloy $Al_{0.5}CoCrCuFeNi$

X-ray studies of the dendritic structure in structural states (I)–(III) were carried out on a DRON-2 (Federal State Unitary Enterprise "Institute for Analytical Instrumentation", Saint Petersburg, Russia) serial diffractometer in FeK_α (states (I)) and CuK_α (states (II) and (III)) radiation using a selectively absorbing manganese filter [24]. According to

X-ray diffraction (XRD) data, the branches of dendrites and interdendritic regions had two different face-centred cubic (fcc) crystal structures with very close lattice parameters, while the ratio of the intensities of diffraction reflections indicates the presence of a predominant crystallite orientation in the samples. Taking into account the ratio of the intensities of diffraction reflections in XRD patterns and the estimation of the volume fraction of phases according to metallography data, dendrites correspond to a phase with a lower lattice parameter fcc_1, and the interdendritic region corresponds to a phase, which has a larger lattice parameter fcc_2. The results of X-ray studies are shown in Figures 4 and 5, and Tables 2–4.

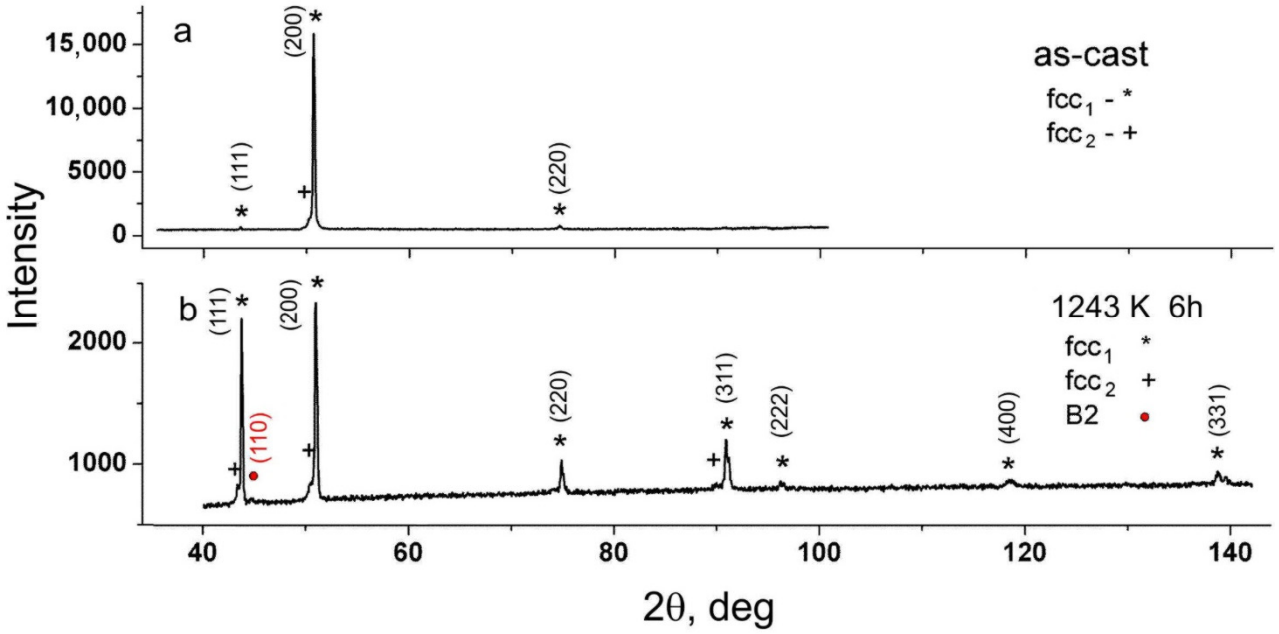

Figure 4. X-ray diffraction patterns of the high-entropy alloy $Al_{0.5}CoCrCuFeNi$: (**a**) initial cast structural state (I); (**b**) after annealing at 1243 K for 6 h—structural state (II).

Table 2. X-ray diffraction data of the $Al_{0.5}CoCrCuFeNi$ HEA in the initial cast structural state (I). The measurements were performed in FeK_α anode radiation, the values of the 2θ angles for CuK_α radiation were obtained by recalculation using the formula $\sin 2\theta_{CuK_\alpha} = \frac{\lambda_{CuK_\alpha}}{\lambda_{FeK_\alpha}} \sin 2\theta_{FeK_\alpha}$; $\lambda_{FeK_\alpha} = 1.937$ Å, $\lambda_{CuK_\alpha} = 1.541$ Å.

Phase	Miller Indices, *hkl*	2θ Angle, deg (FeK_α)	2θ Angle, deg (CuK_α)	Intensity, imp/s	Lattice Parameter *a*, Å
fcc_1	111	55.573	43.56	194.6	3.596
	200	65.079	50.52	14,438.7	
	220	99.183	74.58	220.0	
fcc_2	200	64.568	50.44	791.0	3.625

Table 3. X-ray diffraction data of the $Al_{0.5}CoCrCuFeNi$ HEA in the structural state (II).

Phase	Miller Indices, *hkl*	2θ Angle, deg (CuK_α)	Intensity, imp/s	Lattice Parameter *a*, Å
fcc_1	111	43.672	1551.5	3.588
	200	50.873	1619.0	
	220	74.789	249.5	
	311	90.814	351.7	
	222	96.113	68.7	
	400	118.334	46.7	
	331	138.696	92.2	

fcc_2	111	43.250	139.2	3.620
	200	50.390	123.1	
	311	89.784	45.8	
bcc (type B2)	110	44.610	42.0	2.870

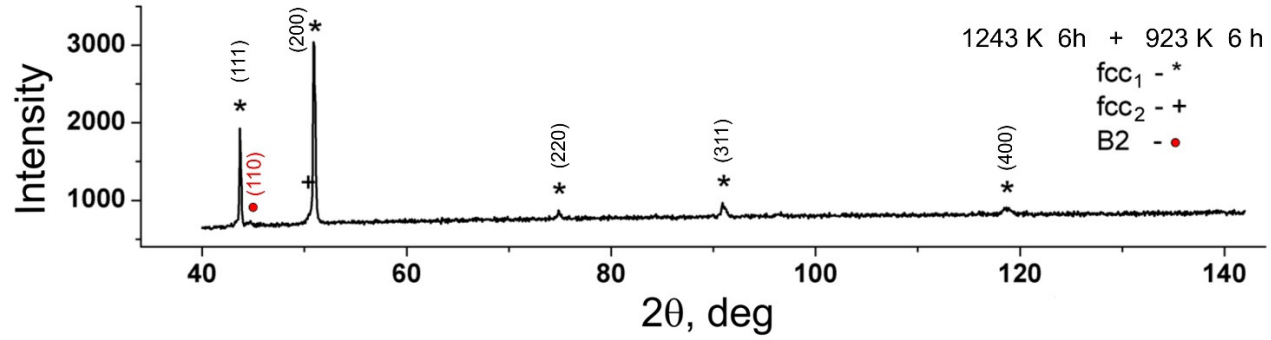

Figure 5. X-ray diffraction patterns of the high-entropy alloy $Al_{0.5}CoCrCuFeNi$ after high-temperature annealing at 1243 K for 6 h with subsequent annealing at 923 K for 6 h—structural state (III).

Table 4. X-ray diffraction data of the $Al_{0.5}CoCrCuFeNi$ HEA in the structural state (III).

Phase	**Miller Indices, *hkl***	**2θ Angle, deg (CuK_α)**	**Intensity, imp/s**	**Lattice Parameter *a*, Å**
fcc_1	111	43.696	739.5	3.584
	200	50.920	2173.6	
	220	74.859	97.7	
	311	90.901	166.0	
	400	118.565	70.0	
fcc_2	111	43.264	44.4	3.617
	200	50.420	115.7	
bcc (type B2)	110	44.691	51.0	2.865

X-ray diffraction (XRD) measurements for structural state (IV) were performed using a PANalytical X'Pert PRO diffractometer (Malvern Panalytical, Almelo, The Netherlands), renowned for its high angular resolution and suitability for peak broadening analysis. The experiments were conducted at the Institute of Low Temperature and Structure Research, Polish Academy of Sciences. XRD patterns were recorded at room temperature in Bragg-Brentano geometry over 2θ range: from 30° to 120°, with a CuK_α anode radiation.

Figure 6 presents XRD patterns obtained from two different adjacent regions (**A** and **B**) of the alloy sample in structural state (IV). The most characteristic reflections are marked with the corresponding Miller indices.

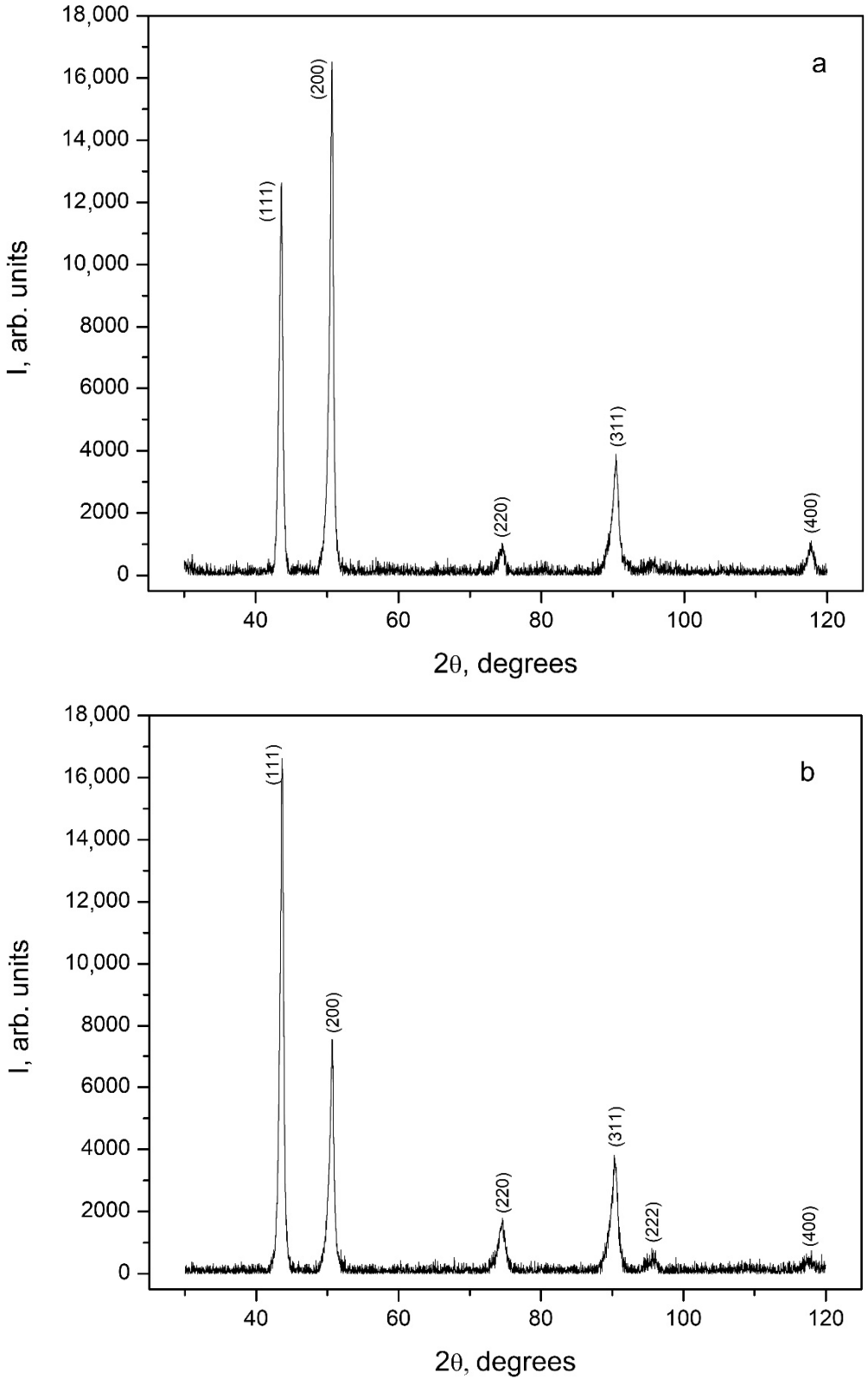

Figure 6. The XRD patterns of two samples (**A** and **B**) cut from different adjacent regions of a high-entropy alloy $Al_{0.5}CoCrCuFeNi$ sample in structural state (IV): (**a**,**b**)—pattern for two different regions (**A** and **B**, respectively).

Table 5 summarizes the results of diffraction patterns processing in structural state (IV) (see Figure 6). It was found that the XRD patterns contain reflections from a single fcc_1 lattice with an average lattice parameter of $\bar{a} = 3.605$ Å. In the structural state (IV), the phases fcc_1 and bcc present in the state (II) are not identified. The observed disappearance of the bcc phase in the $Al_{0.5}CoCrCuFeNi$ high-entropy alloy after 10 years of exposure at room temperature may be attributed to the metastable nature of the bcc phase formed during the initial processing state (II). Over extended time scales, extremely slow atomic diffusion—even at ambient conditions—could facilitate a gradual transformation toward

a more thermodynamically stable fcc structure or lead to phase homogenization. This suggests long-term structural relaxation processes may occur in high-entropy alloys without external thermal activation. So, the disappearance of the bcc phase in the $Al_{0.5}CoCrCuFeNi$ alloy after 10 years at room temperature may indicate a slow diffusion-driven transformation toward a more thermodynamically stable configuration. Previous studies have shown that HEAs often form metastable phases during rapid solidification or mechanical processing, which may gradually evolve over time even without thermal activation [1,5,10]. The high configurational entropy and lattice distortion in these alloys suppress fast diffusion, but do not eliminate it entirely. Thus, extremely slow atomic rearrangements may lead to phase homogenization or transformation, even at ambient conditions. The long-term structural evolution of HEAs remains an area of active investigation.

Table 5. The result of the XRD patterns analysis of $Al_{0.5}CoCrCuFeNi$ HEA in the structural state (IV).

Sample	Miller Indices, *hkl*	2θ Angle, deg	Interplanar Spacing *d*, Å	FWHM, Degrees	Intensity, imp/s	Area	Average Parameter *a*, Å
A see Figure 6a	111	43.507	2.078	0.61	8774	7890.76	3.604
	200	50.580	1.803	0.55	11,139	9634.35	
	220	74.340	1.275	1.10	615	1116.99	
	311	90.270	1.087	0.98	2518	3973.00	
	400	117.540	0.900	1.10	685	1134.59	
B see Figure 6b	111	43.560	2.076	0.57	11,146	9074.80	3.606
	200	50.560	1.804	0.68	4998	5363.54	
	220	74.420	1.274	1.09	1082	1772.99	
	311	90.220	1.087	1.08	2506	4241.30	
	222	95.480	1.040	1.80	309	590.32	
	400	117.30	0.902	1.38	197	496.60	

Data of scanning electron microscopy using an X-ray microanalyser [24] (see Figure 7 and Table 6) show that the elemental composition of dendrites and interdendritic spaces is significantly different.

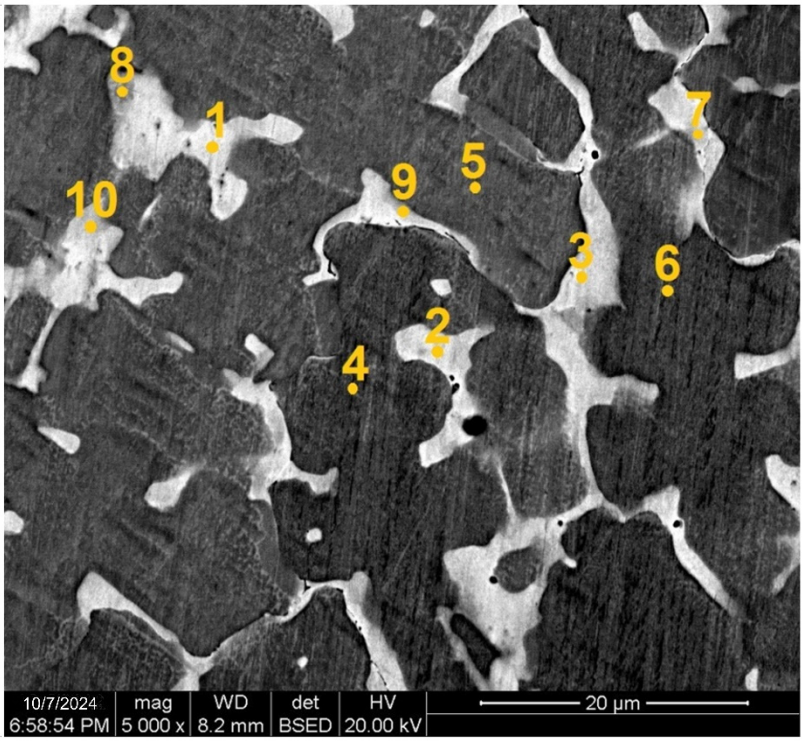

Figure 7. The data of scanning electron microscopy using an X-ray microanalyser for $Al_{0.5}CoCrCuFeNi$ HEA in the initial cast state (I). Points 1–10 denote the measurement sites used for chemical composition analysis.

Table 6. Chemical composition of high-entropy alloy $Al_{0.5}CoCrCuFeNi$ in the initial cast structural state (I) according to X-ray microanalysis data.

Region	Point of Scanning	Chemical Element					
		Al, at %	Cr, at %	Fe, at %	Co, at %	Ni, at %	Cu, at %
interdendritic region, fcc_2	1	14.61	3.18	3.66	3.92	10.08	64.55
	2	14.30	2.69	3.29	3.50	8.81	67.40
	3	14.61	3.38	4.02	4.38	11.25	62.37
boundary between dendrites and interdendritic region	7	15.27	7.46	7.85	7.96	15.98	45.47
	9	15.66	8.23	7.86	7.80	14.06	46.38
	10	16.42	5.73	6.24	6.43	15.45	49.72
unidentified region	8	13.98	13.55	13.58	13.45	19.21	26.23
dendrites, fcc_1	4	8.78	21.74	21.13	20.61	17.83	9.91
	5	7.81	22.59	22.25	21.67	16.84	8.83
	6	7.92	22.60	22.12	21.28	17.03	9.05

The dendrites composition (points **4**, **5**, **6** in Figure 7) is enriched in iron, chromium, and cobalt by more than 20 at.% of each element and depleted in copper and aluminium less than 10 at.%. The interdendritic spaces (points **1**, **2**, **3** in Figure 7) are enriched in copper up to 65 at.% and contain a small amount (less than 4 at.%) of iron, chromium, and cobalt. The aluminium content in the interdendritic spaces is greater (about 15 at.%), which leads to an increase in the fcc lattice parameter. In addition, at the boundary between dendrites and interdendritic region, separate spaces are observed (points **7**, **9**, **10** in Figure 7) to be close in composition to the interdendritic region, but containing less copper and a higher amount of nickel, iron, chromium, and cobalt. Point **8** unidentified region, likely precipitates of intermetallic phases Al_2FeCo and AlNi, with chromium incorporated as a substituting element.

The diffraction pattern of the sample after annealing at 1243 K for 6 h (see Figure 4b and Table 3) showed the presence of two fcc phases (fcc_1 and fcc_2), as well as traces of the bcc phase (type B2).

As a result, it was determined that annealing causes substantial alterations in the alloy's structure and the chemical composition of its structural regions (see Figure 8 and Table 7).

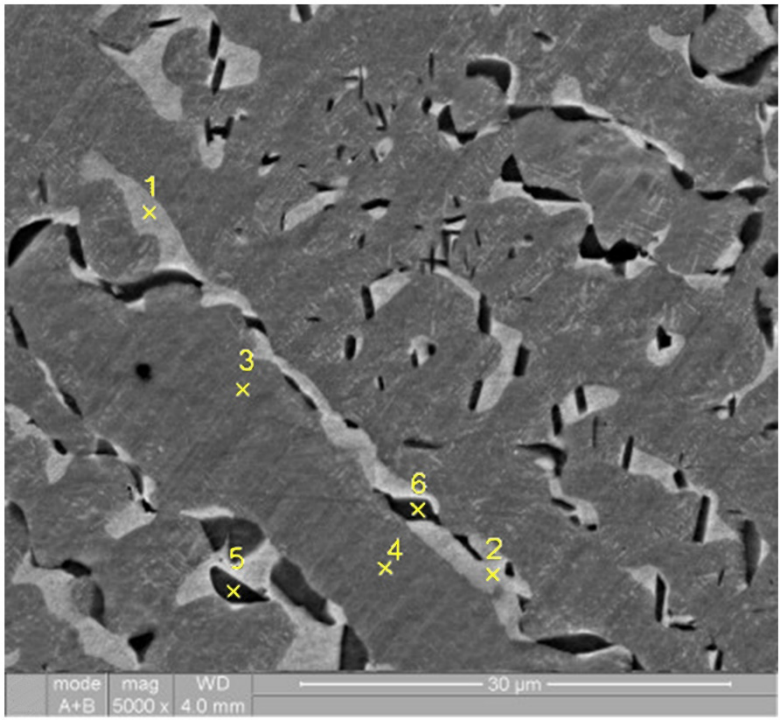

Figure 8. The data of scanning electron microscopy using an X-ray microanalyser for $Al_{0.5}CoCrCuFeNi$ HEA in the structural state (III). Points 1–6 denote the measurement sites used for chemical composition analysis.

The composition of the dendritic regions (points **3** and **4** in Figure 8) remains almost unchanged. In contrast, the interdendritic regions (points **1** and **2** in Figure 8) exhibit a decrease in copper and aluminium content, while the

concentrations of other elements increase. Additionally, bcc phase particles (points **5** and **6** in Figure 8) predominantly form at the boundaries between the dendritic and interdendritic regions, enriched with nickel ≈ 30%, aluminium > 20%, and copper >2 0%.

Table 7. Chemical composition of high-entropy alloy $Al_{0.5}CoCrCuFeNi$ in the structural state (III) according to X-ray microanalysis data.

Region	Point of Scanning	Chemical Element					
		Al, at %	Cr, at %	Fe, at %	Co, at %	Ni, at %	Cu, at %
interdendritic region,	1	8.92	6.39	6.37	6.28	15.48	56.56
fcc_2	2	7.51	6.21	5.88	5.79	12.55	62.05
bcc	5	21.07	6.34	8.99	11.31	30.03	22.26
(type B2)	6	21.44	7.03	8.32	10.09	25.23	27.88
dendrites,	3	5.99	22.39	21.48	20.58	18.17	10.79
fcc_1	4	6.04	21.72	21.22	20.64	18.84	11.54

The elevated concentration of copper in the interdendritic region can be attributed to its relatively high enthalpy of mixing with iron (13 kJ/mol), cobalt (10 kJ/mol) and nickel (4 kJ/mol). This indicates that copper has a low affinity for forming solutions with most of the matrix elements in the system [16,22]. Additionally, the relatively low melting point of copper likely plays a role in this distribution. The differences in melting points also explain the significant difference in chromium concentration between the dendritic and interdendritic regions. Among all elements in the system, chromium possesses the highest melting point, which is significantly greater than that of other alloy components (see Table 1). As a result, Cr-rich regions are capable of solidifying from the melt at the highest temperature.

The distinctive behaviour of nickel stems from its solubility in both phases. With a melting point comparable to iron and cobalt, nickel differs from copper in that it does not exhibit a positive enthalpy of mixing with cobalt, chromium or iron, allowing it to integrate readily into the dendritic phase. Also, nickel is fully soluble in copper, resulting in its higher concentration in the interdendritic region than cobalt, chromium or iron.

This complex interplay between thermodynamic parameters and solidification kinetics governs the elemental partitioning observed in the alloy microstructure. The segregation of copper into the interdendritic regions is further enhanced by its tendency to remain in the liquid phase during solidification, thereby concentrating in the last-to-freeze areas. Conversely, elements with higher melting points and stronger mutual affinities, like chromium and iron, preferentially incorporate into the early-forming dendritic cores.

Moreover, the observed distribution patterns are consistent with the predictions of the Scheil-Gulliver solidification model [29], which assumes negligible diffusion in the solid phase and complete mixing in the liquid. Under such conditions, solute rejection during dendrite growth leads to progressive enrichment of the remaining melt in elements like copper and nickel, which are less compatible with the primary solid phase.

These findings underscore the importance of thermodynamic factors—such as enthalpy of mixing and melting point—and kinetic aspects of solidification in determining the final microstructural architecture of HEAs. Understanding these mechanisms is essential for tailoring alloy compositions and processing conditions to achieve desired phase distributions and mechanical properties.

3.2. Dislocation Structure of the High-Entropy Alloy $Al_{0.5}CoCrCuFeNi$

As seen (Figure 6, Table 5), all reflections have a fairly large width at half peak height (greater than 0.5° in 2θ). The obtaining reflections set was approximated by the Lorentz function. The Bragg peak experimental breadth $\beta_{\exp}$ is a combination of both instrument and sample-dependent effects [30]. To remove these aberrations, a diffraction pattern must be constructed using the line broadening of a standard material to quantify the instrumental broadening. The instrument-corrected physical value of the Full Width at Half Maximum (FWHM) β_{hkl} corresponding to the diffraction peak of the studied alloy was estimated using the relation:

$$\beta_{hkl} = \beta_{\exp} - \beta_{\text{instr}} \quad (5)$$

where $\beta_{\exp}$ is the experimental value of the FWHM of the XRD reflex; β_{instr} is the instrumental value of the FWHM of the X-ray reflection, which was determined based on the instrumental standards for crystallite size estimation.

It's well known that β_{hkl} is affected by not only particle size but also mechanical stresses that arise due to defects in a crystal structure. According to the Williamson-Hall (W-H) model [31,32] broadening β_{hkl} is determined by the additive contribution of crystallite size β_D and the lattice microstrain β_S :

$$\beta_{hkl} = \beta_D + \beta_S \tag{6}$$

As is generally accepted, the contribution to broadening of crystallite size β_D is determined by the Debye–Scherrer equation [33]:

$$\beta_D = \frac{K\lambda}{D\cos\theta} \tag{7}$$

λ is the X-ray wavelength; K is a dimensionless shape factor, with a value close to 1 [33], D is the mean size of the ordered (crystalline) domains, which may be smaller or equal to the grain size, which may be smaller or equal to the particle size (crystallite size); θ is the Bragg angle.

Crystal imperfections and distortion of strain-induced peak broadening within the uniform deformation model are related by $\langle\varepsilon\rangle \propto \frac{\beta_S}{\tan\theta}$:

$$\beta_S = 4\langle\varepsilon\rangle\tan\theta = 4\langle\varepsilon\rangle\frac{\sin\theta}{\cos\theta} \tag{8}$$

where $\langle\varepsilon\rangle$ is the mean square lattice micro strain. Thus

$$\beta_{hkl} = \beta_D + \beta_S = \frac{K\lambda}{D\cos\theta} + 4\langle\varepsilon\rangle\tan\theta \quad \Rightarrow \quad \frac{\beta_{hkl}\cdot\cos\theta}{\lambda} = \frac{K}{D} + \frac{4\langle\varepsilon\rangle\cdot\sin\theta}{\lambda} \tag{9}$$

There is an extraordinary property of Equation (9) , which has a dependency on the diffraction angle θ. The Debye-Scherrer equation follows only a $\frac{1}{\cos\theta}$ dependency, but not $\tan\theta$ as W-H model. Therefore, both crystallite size and strain can be estimated by plotting $\frac{\beta_{hkl}\cdot\cos\theta}{\lambda}$ against $\frac{4\cdot\sin\theta}{\lambda}$ (β_{hkl} in radian and θ in degree) for all the peaks and fitting the best line, the intercept and slope of the fitting line are $\frac{K}{D}$ and $\langle\varepsilon\rangle$, respectively. Figure 9 shows the W-H plot for the specimens of the high-entropy alloy $Al_{0.5}CoCrCuFeNi$ in structural state (IV).

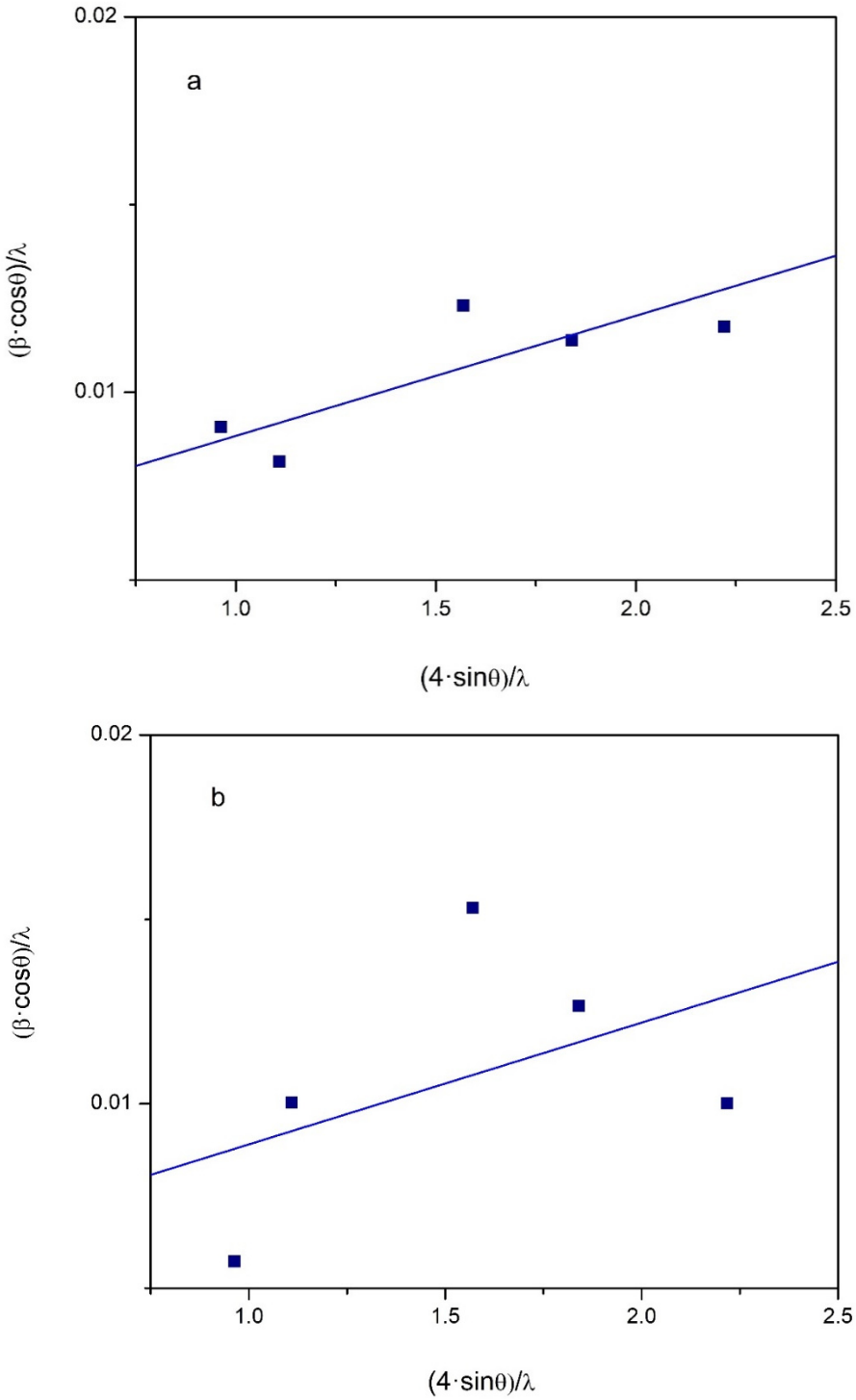

Figure 9. Williamson–Hall plot for the specimens of the high-entropy alloy $Al_{0.5}CoCrCuFeNi$ in structural state (IV): (**a**) is part **A** of the sample; (**b**) is part **B**.

The W-H analysis leads to the following empirical estimates: mean size of the ordered crystalline domains (particle size or coherent scattering regions) $D^{A} = 17.7305$ nm, $D^{B} = 17.857$ nm and average value $\bar{D} \simeq 18$ nm; lattice micro strain $\langle \varepsilon \rangle^{A} = 3.2 \cdot 10^{-3}$, $\langle \varepsilon \rangle^{B} = 3.3 \cdot 10^{-3}$ and average value $\langle \bar{\varepsilon} \rangle = 3.25 \cdot 10^{-3}$. The small size of the experimentally observed regions of coherent scattering in a coarse-grained sample may indicate the presence of a large number of low-angle boundaries. The role which can be played by the boundaries of clusters with the same chemical composition; such nanosized clusters were experimentally observed in the works [13,15].

Both of these parameters, obtained from W-H analysis, may be used for calculating the dislocation density [33]. The dislocation density calculated from the particle size will be determined by the ratio:

$$\rho_D = \frac{3n}{D^2} \tag{10}$$

where n is the number of dislocations per block face, the value of n must be determined or assumed. For our calculation we take $n = 1$; this value represents the minimum density of edge dislocations and is applicable to a structural state where the dislocations are almost randomly distributed [32].

The dislocation density, determined from the strain broadening, is

$$\rho_S = \frac{k}{F} \cdot \frac{\langle \varepsilon \rangle^2}{b^2} \tag{11}$$

the coefficient k lies in the range 2 to 25. For the broadening effect caused by a screw dislocation $k = 16.1$ [33] for fcc lattice with Burgers vector **b** along [110]. Equation (11) can only be applied to the experimental results if the interaction factor F is either known or assumed. The interaction factor $F = 1$ [33], assuming that each dislocation aligns with the edge of a block. In this case, the dislocations are maximally separated, minimizing their interaction. Relations (10) and (11) lead to the following empirical estimates: $\rho_D^A = 9.543 \cdot 10^{15}\ \mathrm{m}^{-2}$, $\rho_S^A = 2.53 \cdot 10^{15}\ \mathrm{m}^{-2}$; $\rho_D^B = 9.4 \cdot 10^{15}\ \mathrm{m}^{-2}$, $\rho_S^B = 2.691 \cdot 10^{15}\ \mathrm{m}^{-2}$. For the case $F = n$, the average value of the dislocation density will be determined as the geometric mean:

$$\overline{\rho} = \sqrt{\rho_D \cdot \rho_S} \tag{12}$$

Which leads to the following estimates for the studied samples of the high-entropy alloy $Al_{0.5}CoCuNiFe$: $\rho^{\mathrm{A}} = 4.914 \cdot 10^{15}\,\mathrm{m}^{-2}$, $\rho^{\mathrm{B}} = 5.031 \cdot 10^{15}\,\mathrm{m}^{-2}$ and $\overline{\rho} = 4.97 \cdot 10^{15}\,\mathrm{m}^{-2}$.

Although the conventional W-H method was employed to estimate microstrain and crystallite size, the relatively poor linear fitting suggests that the strain distribution may be non-uniform. Modified W-H approaches, such as the Uniform Deformation Model (UDM), Uniform Stress Deformation Model (USDM), and Uniform Deformation Energy Density Model (UDEDM), could provide more accurate and physically meaningful estimates [34]. However, due to the limited number of diffraction peaks available in this study, the application of these models did not yield statistically reliable results. Future work involving more comprehensive diffraction data may allow for the implementation of these advanced methods.

Rietveld refinement, while widely recognized for its robustness in extracting detailed crystallographic information, was not employed in this study primarily due to the insufficient number of well-resolved diffraction peaks. As noted in previous literature, the reliability of Rietveld analysis significantly depends on the availability of a rich and high-quality diffraction pattern, typically containing numerous overlapping reflections that can be modeled simultaneously [35]. In our case, the limited peak count and relatively low signal-to-noise ratio would have introduced substantial uncertainty into the refinement process, potentially leading to misleading structural interpretations [36]. Nevertheless, the diffraction data were acquired using the high-resolution PANalytical X'Pert PRO diffractometer, which offers excellent angular precision and peak definition. This instrument is well-suited for microstructural analysis, including peak broadening studies and phase identification, and has been successfully used in similar investigations of nanocrystalline and multiphase materials [37]. Its capabilities, such as the Bragg-Brentano geometry and high-speed X'Celerator detector (Malvern Panalytical, Almelo, The Netherlands), ensured the reliability of the peak positions and widths used in our W-H analysis.

In future studies, the use of extended scan ranges, longer acquisition times, and complementary techniques such as synchrotron radiation or neutron diffraction may help overcome current limitations and enable full-profile Rietveld refinement with greater confidence.

An estimate $\sim 4 \cdot 10^{13}\ \mathrm{m}^{-2}$ of the total length of dislocation segments per unit volume was obtained within the Koiwa-Hasiguti model for the relaxation process of sound absorption at $T_p = 228\ \mathrm{K}$ [28]. The obtained value is less than the value $\sim 5 \cdot 10^{15}\ \mathrm{m}^{-2}$ of total dislocation density obtained by the X-ray diffraction analysis. This observation aligns with the well-established concept that a substantial portion of dislocations tends to accumulate along grain boundaries, where they contribute to localized strain fields but remain largely inactive in terms of dynamic mechanical response. In contrast, only those dislocation segments situated within the grain interiors—and possessing a favorable crystallographic orientation relative to the direction of acoustic wave propagation—are capable of effectively coupling with the cyclic deformation of the sample. These intragranular dislocations can resonate with the elastic vibrations,

thereby influencing the internal friction and energy dissipation mechanisms observed during mechanical spectroscopy. Their selective activation underscores the anisotropic nature of dislocation mobility and highlights the importance of microstructural configuration in determining the material's dynamic mechanical behavior.

It is well established that alloying elements such as Al, Cr, and Cu tend to form solid solutions or intermetallic compounds in multi-component systems. These phases can act as dislocation pinning centers, thereby hindering dislocation annihilation during annealing and contributing to the retention of strain hardening. For example [38], in Al-Cu systems, prolonged annealing leads to the formation of Al_2Cu and Al_4Cu_9 intermetallics, which are known to influence dislocation behavior and mechanical strength at the interface. Similarly, Cr-containing alloys often exhibit stable intermetallic phases that resist recovery processes. These effects are particularly pronounced in high-entropy alloys, where the combination of lattice distortion and chemical complexity stabilizes dislocation structures [10]. Cu-enriched regions were identified in our investigation and in [39], where a high-entropy alloy of similar composition was studied. Furthermore, in our previous research on the acoustic properties of the $Al_{0.5}CoCrCuFeNi$ HEA, we established that, in addition to a relatively high dislocation density, a significant number of dislocation pinning sites were present. The typical dislocation segment length was found to be on the order of 10–20 nm [28]. These observations strongly suggest that one of the most probable reasons for the retention of a relatively high dislocation density in the annealed sample (structural state (IV)) is the effective pinning of dislocations by atomic clusters with elevated Cu content. This mechanism may play a key role in stabilizing the microstructure and influencing the mechanical behavior of the alloy after annealing.

4. Conclusions

A comprehensive analysis of the structure of the high-entropy alloy $Al_{0.5}CoCrCuFeNi$ at room temperature was carried out using various methods of electron microscopy and X-ray structural analysis techniques.

It was found that the initial ingots of the studied alloy have a dendritic structure, which is formed during the creation of ingots by the argon-arc method with directed heat removal. The chemical composition and structure of dendrites and interdendritic region and their evolution during annealing were studied. It was observed that the composition of dendritic regions remains virtually unchanged, whereas in the interdendritic regions, the concentrations of copper and aluminium decrease while the content of other elements increases. Predominantly at the boundaries between dendritic and interdendritic regions, areas enriched with Ni, Al, and Cu tend to form. Additionally, due to structural-phase transformations, the bcc phase is released within the fcc matrix.

It was found that during prolonged annealing, the alloy under study becomes single-phase with an fcc lattice.

This transformation is accompanied by a homogenization of the chemical composition and a reduction in internal stresses, which contributes to the stabilization of the microstructure. The observed phase evolution is consistent with thermodynamic predictions for multi-component systems and highlights the metastable nature of the initial as-cast state.

Numerical estimates of the dislocation density $\sim 5 \cdot 10^{15}\ \mathrm{m}^{-2}$, the mean size of the ordered (crystalline) clusters ~ 18 nm and lattice micro strain $\sim 3 \cdot 10^{-3}$ were obtained through Williamson-Hall analysis of XRD patterns. The obtained estimates correlate with the estimates of the density of dislocations effectively interacting with the elastic vibrations of the sample, which were determined by the method of resonance mechanical spectroscopy. These complementary techniques provide a coherent picture of the defect structure and its evolution during thermal treatment, confirming the reliability of the microstructural interpretation.

Furthermore, the presence of residual microstrain and the distribution of dislocations suggest that the alloy retains a degree of internal heterogeneity even after annealing, which may influence its mechanical behavior under load. These findings are crucial for understanding the relationship between processing conditions, microstructure, and functional properties of high-entropy alloys, especially in the context of their application in load-bearing and high-temperature environments.

Acknowledgments

The authors express their sincere gratitude to Damian Szymański for his valuable contribution to this work through the precise elemental composition analysis of the high-entropy alloy (HEA) $Al_{0.5}CoCrCuFeNi$. His expertise in spectroscopic techniques and meticulous approach to data acquisition played a crucial role in ensuring the reliability and accuracy of the chemical characterization, which served as a foundation for subsequent structural and microstructural investigations.

Author Contributions

Conceptualization, Y.S. and V.N.; Methodology, Y.S., N.G., D.H. V.Z.; Validation, Y.S., V.N. and E.T.; Formal Analysis, V.Z. and P.Z.; Investigation, Y.S., N.G., D.H., T.B. and I.K.; Resources, N.G. and D.H.; Data Curation, E.T.; Writing—Original Draft Preparation, Y.S.; Writing—Review & Editing, Y.S. and V.N.; Visualization, V.Z. and Y.S.; Supervision, X.X.; Project Administration, Y.S.; Funding Acquisition, V.N. and E.T.

Ethics Statement

Not applicable

Informed Consent Statement

Not applicable

Data Availability Statement

The data presented in this study are available upon request from the corresponding author.

Funding

This work was partly supported by the NRFU (Grant 2023.03/0012); Projects No.0122U001504 and No.0124U000272 NAS of Ukraine and internship within the framework of scientific cooperation between the National Academy of Sciences of Ukraine and the Polish Academy of Sciences.

Declaration of Competing Interest

The authors declare no conflicts of interest.

References

1. Yeh JW, Chen SK, Lin SJ, Gan JY, Chin TS, Shun TT, et al. Nanostructured High-Entropy Alloys with Multiple Principal Elements: Novel Alloy Design Concepts and Outcomes. *Adv. Eng. Mater*. **2004**, *6*, 299–303. doi:10.1002/adem.200300567.
2. Cantor B, Chang ITH, Knight P, Vincent AJB. Microstructural development in equi-atomic multi-component alloys. *Mater. Sci. Eng*. **2004**, *A 375–377*, 213–218. doi:10.1016/j.msea.2003.10.257.
3. Zhang Y, Zhou YJ, Lin JP, Chen GL, Liaw PK. Solid-solution phase formation rules for multi-component alloys. *Adv. Eng. Mater*. **2008**, *10*, 534–538. doi:10.1002/adem.200700240.
4. George EP, Raabe D, Ritchie RO. High-entropy alloys. *Nat. Rev. Mater*. **2019**, *4*, 515–534. doi:10.1038/s41578-019-0121-4.
5. Zhang Y, Zuo TT, Tang Z, Gao MC, Dahmen KA, Liaw PK, et al. Microstructures and properties of high-entropy alloys. *Progr. Mat. Sci*. **2014**, *61*, 1–93. doi:10.1016/j.pmatsci.2013.10.001.
6. Pogrebnjak AD, Yakushchenko IV, Bagdasaryan AA, Bondar OV, Krause-Rehberg R, Abadias G, et al. Microstructure, physical and chemical properties of nanostructured (Ti–Hf–Zr–V–Nb) N coatings under different deposition conditions. *Mater. Chem. Phys*. **2014**, *147*, 1079–1091. doi:10.1016/j.matchemphys.2014.06.062.
7. Pogrebnjak AD, Bagdasaryan AA, Yakushchenko IV, Beresnev VM. The structure and properties of highentropy alloys and nitride coatings based on the, *Russ. Chem. Rev*. **2014**, *83*, 1027–1061. doi:10.1070/RCR4407.
8. Tsai MH, Yeh JW. High-entropy alloys: A critical review, *Mat. Res. Let*. **2014**, *2*, 107–123. doi:10.1080/21663831.2014.912690.
9. Zhou YJ, Zhang Y, Wang YL, Chen GL. Solid solution alloys of $AlCoCrFeNiTi_x$ with excellent room-temperature mechanical properties. *Appl. Phys. Lett.* **2007**, *90*, 181904. doi:10.1063/1.2734517.
10. Miracle DB, Senkov ON. A critical review of high entropy alloys and related concepts, *Acta Mater*. **2017**, *122*, 448–511. doi:10.1016/j.actamat.2016.08.081.
11. Guo S, Liu CT. Phase stability in high entropy alloys: formation of solid-solution phase or amorphous phase. *Prog. Nat. Sci. Mater.* **2011**, *21*, 433–446. doi:10.1016/S1002-0071(12)60080-X.
12. Tong C-J, Chen Y-L, Yeh J-W, Lin S-J, Chen S-K, Shun T-T, et al. Microstructure characterization of $Al_xCoCrCuFeNi$ high-entropy alloy system with multiprincipal elements. *Metall. Mater. Trans.* **2005**, *36*, 881–893. doi:10.1007/s11661-005-0283-0.
13. Xu XD, Guo S, Nieh TG, Liu CT, Hirata A, Chen MW. Effects of mixing enthalpy and cooling rate on phase formation of $Al_xCoCrCuFeNi$ high-entropy alloys. *Materialia* **2019**, *6*, 100292. doi:10.1016/j.mtla.2019.100292.
14. Tsai CW, Tsai MH, Yeh JW, Yang CC. Effect of temperature on mechanical properties of $Al_{0.5}CoCrCuFeNi$ wrought alloy. *J.*

Alloys Compd. **2010**, *490*, 160–165. doi:10.1016/j.jallcom.2009.10.088.
15. Hsu YJ, Chiang WC, Wu JK. Corrosion behavior of $FeCoNiCrCu_x$ high-entropy alloys in 3.5% sodium chloride solution. *Mater. Chem. Phys.* **2005**, *92*, 112–117. doi:10.1016/j.matchemphys.2005.01.001.
16. Novak TG, Vora HD, Mishra RS, Young ML, Dahotre NB. Synthesis of $Al_{0.5}CoCrCuFeNi$ and $Al_{0.5}CoCrFeMnNi$ High-Entropy Alloys by Laser Melting. *Metall Mater. Trans.* **2014**, *B45*, 1603–1607. doi:10.1007/s11663-014-0170-4.
17. Han F, Li C, Huang J, Wang J, Xue L, Wang C, et al. Research Advances in Additively Manufactured High-Entropy Alloys: Microstructure, Mechanical Properties, and Corrosion Resistance. *Metals* **2025**, *15*, 136. doi:10.3390/met15020136.
18. Chowdhury S, Yadaiah N, Prakash C, Ramakrishna S, Dixit S, Gupta LR, et al. Laser powder bed fusion: A state-of-the-art review of the technology, materials, properties & defects, and numerical modelling. *J. Mater. Res. Technol.* **2022**, *20*, 2109–2172. doi:10.1016/j.jmrt.2022.07.121.
19. Tan C, Li R, Su J, Du D, Du Y, Attard B, et al. Review on field assisted metal additive manufacturing. *Int. J. Mach. Tools Manuf.* **2023**, *189*, 104032. doi:10.1016/j.ijmachtools.2023.104032.
20. Ron T, Shirizly A, Aghion E. Additive Manufacturing Technologies of High Entropy Alloys (HEA): Review and Prospects. *Materials* **2023**, *16*, 2454. doi:10.3390/ma16062454.
21. Murad Ali K. High-Entropy Alloys: Recent Developments and Future Perspectives in Material Science. *JOJ Mater. Sci.* **2025**, *9*, 555760. doi:10.19080/JOJMS.2025.09.555760.
22. Pickering EJ, Stone HJ, Jones NG. Fine-scale precipitation in the high-entropy alloy Al0.5CrFeCoNiCu. *Mat. Sci. Eng.* **2015**, *A645*, 65–71. doi:10.1016/j.msea.2015.08.010.
23. Laktionova MO, Tabachnikova OD, Tang Z, Liaw PK. Mechanical properties of the high-entropy alloy $Al_{0.5}CoCrCuFeNi$ at temperatures of 4.2–300 K. *Low Temp. Phys.* **2013**, *39*, 630–632. doi:10.1063/1.4813688.
24. Semerenko YO, Tabachnikova OD, Tikhonovska TM, Kolodiy IV, Tortika OS, Shumilin SE, et al. Temperature Dependence of the Acoustic and Mechanical Properties of Cast and Annealed High-Entropy $Al_{0.5}CoCuCrNiFe$ Alloy. *Metallofiz. Noveishie Tekhnol.* **2015**, *37*, 1527–1538. (In Russian)
25. Tabachnikova ED, Laktionova MA, Semerenko YA, Shumilin SE, Podolskiy AV, Tikhonovsky MA, et al. Mechanical properties of $Al_{0.5}CoCrCuFeNi$ high entropy alloy in different structural states in temperature range 0.5–300 K. *Low Temp. Phys.* **2017**, *43*, 1108–1118. doi:10.1063/1.5004457.
26. Semerenko YA, Natsik VD. Low temperature peak of internal friction in high entropy $Al_{0.5}CoCrCuFeNi$ alloy. *Low Temp. Phys.* **2020**, *46*, 78–86. doi:10.1063/10.0000367.
27. Semerenko Y, Natsik V, Tabachnikova ED, Huang Y, Langdon TG. Mechanisms of Low-Temperature Dislocation Motion in High-Entropy $Al_{0.5}CoCrCuFeNi$ Alloy. *Metals* **2024**, *14*, 778. doi:10.3390/met14070778.
28. Natsik VD, Semerenko YO, Tabachnikova ED. Dislocation mechanisms of acoustic relaxation and plastic deformation of a high-entropy alloy $Al_{0.5}CoCrCuFeNi$ under moderate to deep cooling conditions: Experiment and theory (Review). *Low Temp. Phys.* **2025**, *51*, 282–299. doi:10.1063/10.0035810.
29. Pelton AD, Eriksson G, Bale CW. Scheil–Gulliver Constituent Diagrams. *Metall. Mater. Trans.* **2017**, *A 48*, 3113–3129. doi:10.1007/s11661-017-4059-0.
30. Mirkin LI. *Handbook of X-ray Analysis of Polycrystalline Material*; Consultants Bureau: New York, NY, USA, 1964; 31p.
31. Williamson GK, Hall WH. X-ray line broadening from filed aluminium and wolfram. *Acta Met.* **1953**, *1*, 22–31. doi:10.1016/0001-6160(53)90006-6.
32. Williamson GK, Smallman RE, III. Dislocation densities in some annealed and cold-worked metals from measurements on the X-ray Debye-Scherrer spectrum. *Phil. Mag.* **1956**, *1*, 34–46. doi:10.1080/14786435608238074.
33. Patterson A. The Scherrer Formula for X-Ray Particle Size Determination. *Phys. Rev.* **1939**, *56*, 978–982. doi:10.1103/PhysRev.56.978.
34. Prabhu YT, Rao KV, Kumar VSS, Kumari BS. X-ray Analysis by Williamson-Hall and Size-Strain Plot Methods of ZnO Nanoparticles with Fuel Variation. *World J. Nano Sci. Eng.* **2014**, *4*, 21–28. doi:10.4236/wjnse.2014.41004.
35. Young RA. *The Rietveld Method*; Oxford University Press: Oxford, UK, 1993.
36. Altomare A, Capitelli F, Corriero N, Cuocci C, Falcicchio A, Moliterni A, et al. The Rietveld Refinement in the EXPO Software: A Powerful Tool at the End of the Elaborate Crystal Structure Solution Pathway. *Crystals* **2018**, *8*, 203. doi:10.3390/cryst8050203.
37. Nanousers Facility. (n.d.). PANalytical X'Pert PRO Diffractometer. Massachusetts Institute of Technology. Available online: https://nanousers.mit.edu/characterizenano/focus-facilities/xray-diffraction/panalytical-xpert-pro (accessed on 1 September 2025).
38. Wang X, Cheng G, Zhang Y, Wang Y, Liao W, Venkatesh TA. On the Evolution of Nano-Structures at the Al–Cu Interface and the Influence of Annealing Temperature on the Interfacial Strength. *Nanomaterials* **2022**, *12*, 3658. doi:10.3390/nano12203658.
39. Wen LH, Kou HC, Li JS, Chang H, Xue XY, Zhou L. Effect of aging temperature on microstructure and properties of AlCoCrCuFeNi high-entropy alloy. *Intermetallics* **2009**, *17*, 266–269. doi:10.1016/j.intermet.2008.08.012.